NANO LETTERS

Letter

pubs.acs.org/NanoLett

# Second-Harmonic Generation from Metal Nanoparticles: Resonance Enhancement versus Particle Geometry

Robert Czaplicki,*[,†] Jouni Mäkitalo,[†] Roope Siikanen,[†] Hannu Husu,[†] Joonas Lehtolahti,[‡] Markku Kuittinen,[‡] and Martti Kauranen[†]

[†]Department of Physics, Tampere University of Technology, P.O. Box 692, FI-33101 Tampere, Finland

[‡]Institute of Photonics, University of Eastern Finland, P.O. Box 111, FI-80101 Joensuu, Finland

Supporting Information

**ABSTRACT:** We demonstrate that optical second-harmonic generation (SHG) from arrays of noncentrosymmetric gold nanoparticles depends essentially on particle geometry. We prepare nanoparticles with different geometrical shapes (L and T) but similar wavelengths for the polarization-dependent plasmon resonances. In contrast to recent interpretations emphasizing resonances at the fundamental frequency, the T shape leads to stronger SHG when only one, instead of both, polarization component of the fundamental field is resonant. This is explained by the character of plasmon oscillations supported by the two shapes. Our numerical simulations for both linear and second-order responses display unprecedented agreement with measurements.

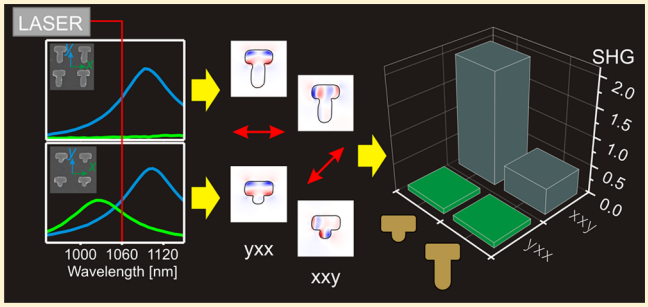


**KEYWORDS:** *Metal nanoparticles, nonlinear optics, second-harmonic generation, plasmonic resonances*

The interaction of light with metal nanoparticles can be described in terms of collective oscillations of conduction electrons, giving rise to localized surface plasmon resonances (LSPRs).[1] The properties of LSPRs can be tuned widely by changing the size, shape, and dielectric environment of the particles.[2] When the particles are arranged in arrays, the overall response is also affected by the coupling between the individual particles.[3−6]

An important consequence of LSPRs is the strong enhancement of the local electromagnetic fields ("hot spots"), which can boost nonlinear optical effects in nanostructures.[7,8] One of the nonlinear effects that can be enhanced is second-harmonic generation (SHG), which converts two photons at a fundamental frequency into one photon at the doubled frequency. As an even-order nonlinear process, SHG is limited by the noncentrosymmetry requirement of the material structure. This condition is most convenient to achieve with structures that look noncentrosymmetric even when viewed at normal incidence. The samples can then be investigated at normal incidence, such that the incoming and outgoing optical fields have components mostly in the sample plane. This ensures that the fields would not couple to the (traditional) surface nonlinearity of, for example, a bare sample substrate, which has a strong out-of-plane character. In consequence, the nonlinear responses must arise from the designed symmetry of the nanostructure.

A large variety of noncentrosymmetric metal nanostructures have been investigated by SHG during the past decade, including L-shaped,[9,10] T-shaped,[11] and G-shaped[12−14] particles, split-ring resonators (SRRs),[15] dimers,[16,17] oligomers,[18] nanocups,[19] or even more complicated shapes.[20] The importance of LSPRs at the fundamental[20−24] and/or second-harmonic frequency[20,22−24] has also been emphasized. The strong nonlinear response requires a LSPR at the fundamental frequency,[22] yet it is possible to use resonances at multiple wavelengths.[23] However, the resonance at the second-harmonic frequency has also been considered to be a loss mechanism, at least for the case of gold SRRs.[22]

Importantly, the strong local fields associated with plasmon resonances cannot overcome the noncentrosymmetry requirement. This is particularly evident for nanodimers separated by a nanogap. Nanogaps can give rise to very strong local fields, nevertheless, centrosymmetric dimers suppress SHG very efficiently.[25] In addition, the relation between plasmon resonances, particle symmetry, and associated local-field distributions can be very complicated.[26] Symmetry breaking is also essentially a qualitative concept. It is therefore a completely open question how the geometry of various noncentrosymmetric shapes and their plasmon resonances affect the second-order nonlinear response and how this response can be most efficiently utilized.

In this Letter, we investigate this crucial question by using arrays of noncentrosymmetric nanoparticles of different geometrical shapes and show that their SHG response cannot be understood only in terms of resonance effects. Instead, the

**Received:** October 10, 2014
**Revised:** December 15, 2014
**Published:** December 18, 2014





DOI: 10.1021/nl503901e
*Nano Lett.* 2015, 15, 530−534

directions of plasmon oscillations supported by the particle geometry and associated local-field distributions play an essential role. In order to show this, we prepare arrays with L- and T-shaped particles, both having at least one resonance close to the fundamental wavelength. In contrast to earlier interpretations, we find that the strongest SHG responses are not necessarily associated with optimizing the resonances for the fundamental field. In some cases, the resonance conditions need to be compromised in order to obtain a favorable coupling of the plasmonic oscillations to the second-order response.

Our samples consist of arrays of 20 nm thick gold nanoparticles fabricated by standard electron-beam lithography and lift-off techniques. As a substrate, we use a 0.5 mm thick fused silica plate coated with 4 nm thick chromium adhesion layer. The particles are covered by a 20 nm thick protective layer of fused silica. We choose particles of different noncentrosymmetric geometries (L- and T-shapes) that have strongly dichroic resonances for light polarized along the *x*- and *y*-axes as defined in Figure 1. The particles are arranged in

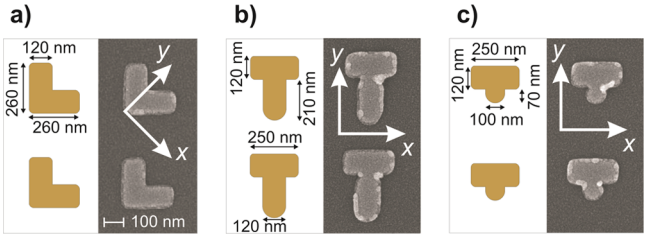


**Figure 1.** Design and scanning electron microscopy images of (a) sample L, (b) sample T_b, and (c) sample T_s. The coordinate systems, dimensions, and scale bar are also shown.

square arrays of 500 nm period. The reference sample (sample L) consists of the L-shaped nanoparticles with symmetric arms of width 120 nm and length 260 nm (Figure 1a).[6,10] The T-shaped particles (samples T_b and T_s) have the upper horizontal section of the same geometry, width 120 nm and length 250 nm, but the lower vertical section is different. It is either 120 nm wide and 210 nm long in the case of sample T_b (Figure 1b) or 100 nm wide and 70 nm long in the case of sample T_s (Figure 1c). Such geometries result in either *x*- or *y*-polarized resonances or both to be near the wavelength of the laser used in our SHG experiments (1060 nm).

The linear spectra of the samples were determined by measuring their extinction at normal incidence for *x* and *y* polarizations (Figure 2). Light from a halogen bulb was coupled to an optical fiber and then collimated using a microscope

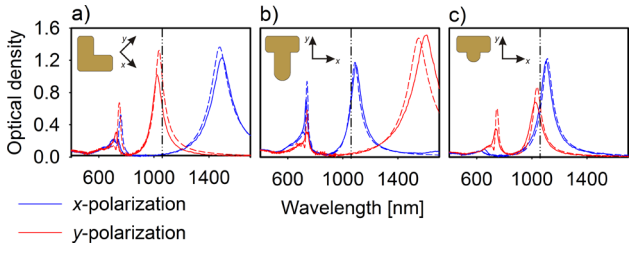


**Figure 2.** Polarized extinction spectra of (a) sample L, (b) sample T_b, and (c) sample T_s. The solid lines denote measured spectra and dashed lines the calculated ones. The fundamental wavelength of our laser (1060 nm) is marked as vertical dash-dotted line. Coordinate systems and particle geometries are shown as insets.

objective and pinhole in front of the sample. The light after the sample was focused to another fiber with a lens and directed to a spectrometer (Avantes AvaSpec-2048 for visible and Avantes NIR256 for infrared spectral range).

Sample L exhibits resonances for *x*- and *y*-polarized light at the wavelengths of 1494 and 1023 nm, respectively. The latter resonance is thus close to the fundamental wavelength of the SHG experiments (1060 nm). Sample T_b also has spectrally well-separated resonances. The *x*-polarized resonance at 1096 nm is now near the fundamental wavelength, but the *y*-polarized resonance is at a longer wavelength (1611 nm). For sample T_s, both resonances are near the fundamental wavelength, the resonance wavelengths being 1105 nm for *x*- and 1023 nm for *y*-polarization. The resonances closest to the laser wavelength do differ somewhat in their strength. However, the laser wavelength is within one-half line width from the line center for each case. All samples have additional resonances at around 760 nm that are related to plasmon oscillations along the width of the arms (L)[27] or sections (T_b, T_s) and to higher order modes.

The SHG measurements were performed in transmission at normal incidence using an Nd:glass laser (200 fs pulses at 1060 nm wavelength, average output power 150 mW, 82 MHz) as a source of fundamental light. The laser beam was weakly focused and its polarization was cleaned with a high-quality Glan polarizer. A half-wave plate was used to change the linear input polarization, while the analyzer in front of the detector allowed only one selected polarization component of the second-harmonic field to be detected.

The symmetry group of all samples is $C_{1v}$, which allows nonvanishing SHG signals for the in-plane components *yyy*, *yxx*, and *xxy* = *xyx* of the nonlinear response tensor,[28] which describes the effective nonlinearity of the whole sample. Here, the first letter refers to the polarization of SHG radiation and the two last letters describe the polarization of the fundamental field. The forbidden tensor components, for example, *xxx* and *xyy*, are very low as are the SHG signals related to them, also indicating high quality of the samples.[10] Note that for the case of mixed input polarizations, the allowed tensor components *yyy* and *yxx*, which can be determined individually by using *y*- or *x*-polarized input light, respectively, give rise to *y*-polarized signals. However, the mixed input polarizations are only used to access the tensor component *xxy* = *xyx* by detecting *x*-polarized light.

The results for SHG measurement are summarized in Figure 3. SHG from arrays of L-shaped gold nanoparticles has been previously studied,[10] thus such a sample is a well-understood reference for the present work. Consequently, the SHG signals in Figure 3 were normalized to the dominant tensor component *yyy* of sample L, for which the polarization of the

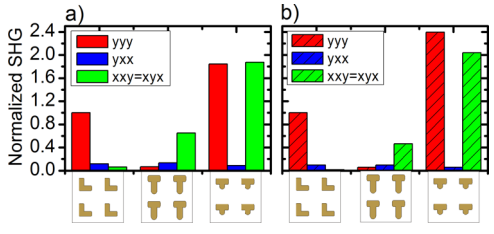


**Figure 3.** (a) Measured and (b) calculated from the near field distribution, SHG signals from studied samples normalized to *yyy* component of sample L.



DOI: 10.1021/nl503901e
*Nano Lett.* 2015, 15, 530−534

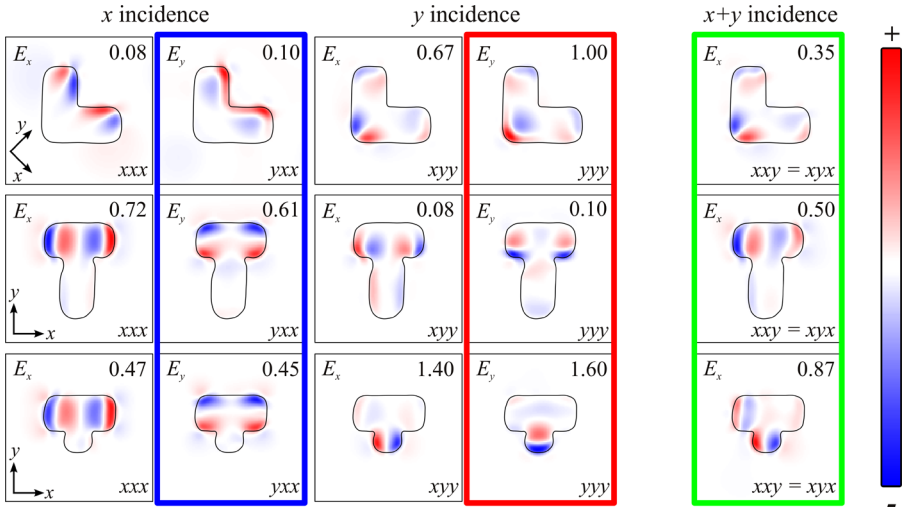


**Figure 4.** *x*- and *y*-polarization components of the near fields at the second-harmonic wavelength calculated at a plane 15 nm after the gold nanoparticles. The shown quantity corresponds to the real part of the field at a moment when the real part of the strongest spot is maximum. Sample L (top row), sample T_b (middle row), and sample T_s (bottom row) for *x*-polarized, *y*-polarized, and *x* + *y* polarized input beam at the fundamental wavelength, respectively. The numbers in the right upper corners show the maximum field amplitudes normalized to that for the *yyy* component of L. The input polarizations are indicated above the figures and the calculated SHG components are shown in the left upper corners. The labels in the right bottom corner show the tensor components that contribute to each panel. The near fields related to allowed tensor components are framed with thick blue, red, and green lines, where the colors represent the colors of SHG signals from Figure 3 (and Figure S2 in Supporting Information).

fundamental wavelength (*y*) is resonant. We thus have a double resonance at the fundamental wavelength in the sense that both field components corresponding to the two last indices of the tensor component are resonant. When the incident polarization is nonresonant (*x*), the allowed component (*yxx*) is very weak. The component with mixed input polarizations (*xxy* = *xyx*, one resonant and one nonresonant), however, is even weaker (Figure 3) as observed also in earlier studies.[6] This result already deviates from the expectation that the resonance characteristics can be used to explain the SHG responses of metal nanostructures.

For sample T_b, the *y*-polarized fundamental wavelength is nonresonant and the allowed component *yyy* is weak. The allowed, doubly resonant component *yxx* is expected to have strong SHG signal if only resonance characteristics and symmetry rules are considered, but this component is weak as well. On the other hand, the fundamental field containing both *x* and *y* components (*xxy* = *xyx*) gives rise to the only strong SHG signal for sample T_b.

The incident field of sample T_s is always resonant since the *x*- and *y*-polarized resonances are close to the wavelength of our laser (see Figure 2c). Hence, all the allowed components are expected to yield strong SHG signals on the basis of resonance considerations. However, only the components *xxy* = *xyx* and *yyy* have strong SHG signals, and these signals are exceptionally strong. The component *yxx*, which is also allowed, however, has a much weaker SHG signal.

At first sight, these results are surprising, because they do not agree with the expectation that plasmonic resonances at the fundamental frequency are beneficial for the nonlinear responses.[22] Focusing solely on resonances, however, neglects an additional important factor that the total SHG response of a particle is obtained by integrating the local response over the particle shape. In consequence, the local-field distributions play an important, yet subtle, role in determining the integrated response. In order to understand the second-harmonic responses from our samples, we model their extinction spectra, SHG local fields and far-field SHG signals using the boundary element method (BEM)[29−38] where we also take into account the periodicity and the substrate.

So as to replicate experimental conditions in the calculations as well as possible, we used the outlines of the particles from the SEM images instead of the ideal shapes to model the geometry. The comparison in Figure 2 between the extinction spectra shows very good quantitative agreement between the measured and simulated results, which is essential for the reliable simulation of the SHG measurements (Figure 3b).

We simulated the SHG from the structures by considering only the dominant susceptibility component $\chi_{nnn}$ of the local response of the metal−air interfaces, where *n* is the direction of the local surface normal.[16,39,40] The generated SHG near fields were calculated on a plane 15 nm from the particle toward the detector. This allows us to intuitively study how the observed overall SHG signals are built up from the local responses. According to the Rayleigh−Sommerfeld diffraction theory

$$S_i = \left| \int E_i dS \right|^2, \quad i = x, y, z$$

where $S_i$ is the far-field signal for the field component *i*, $E_i$ is the respective second-harmonic field component, and the integration is over the plane of Figure 4. We used this equation to arrive at the signals shown in Figure 3b once the near fields had been obtained from the BEM modeling.

This equation also shows that even strong local responses cancel in the total signal if they produce out-of-phase SHG wavelets in the far-field.[25] This occurs when equal hot spots are obtained on symmetrically opposite sides of the particle, where the local surface normals point in opposite directions, and one is interested in the total signal polarized in the direction of this particular surface normal.

Our calculations were performed for the fundamental wavelength of the laser used in the experiment, which is 1060 nm. Note that the results for the overall SHG signals (Figure 3b) exhibit essentially quantitative agreement between the



DOI: 10.1021/nl503901e
*Nano Lett.* 2015, 15, 530−534

experiment and theory for all the samples investigated. The minor differences can be attributed to small deviations in the exact wavelengths and strengths of the plasmon resonances between experiment and modeling. Particularly, such differences can affect the results in the case of sample T_s, where both resonances are close to each other and to the fundamental wavelength. To confirm this, we repeated the calculations for the wavelength 1068 nm where the simulated relative optical densities for the two resonances match better with those for the 1060 nm in the experiment (Supporting Information, Figure S1). The agreement between the experiment and calculations is then even higher (Supporting Information, Figure S2).

The calculated SHG near fields (Figure 4) provide a simple physical interpretation of how the near fields add up in the measured overall signals. The salient features of this approach are easiest to understand by considering the *xxx* component, which is forbidden by symmetry for all samples. Although the *x*-polarized SHG near fields are strong for the two T particles, they are out-of-phase at the left and right ends of the horizontal section, thus interfering destructively in the measured far-field signal.[41]

For sample L, the *x*-polarized input field is nonresonant and the hot spots are weak, giving rise to weak SHG signals (*yxx* component of L in Figure 4). The *y*-polarized input field, oscillating along the arms of the L, results in hot spots at the end of the arms and at the corner of the L. The *y*-component of the latter hot spot (red) is by far the strongest, whereas the out-of-phase parts (blue) remain weak, thus leading to strong *y*-polarized SHG radiation (*yyy* component of L in Figure 4). When the input field is polarized along one of the arms ($x + y$ incidence of L), the hot spots reproduce those for the *y*-polarized input, because only this input component is resonant. However, the *x*-components of these hot spots have essentially symmetric out-of-phase parts, which give rise to only very weak over component $xxy = xyx$, as also evident in Figure 3.

The specific particle geometry of sample T_b and *x*-polarized input field leads to plasmon oscillations mainly along the horizontal section. This gives rise to strong hot spots at the ends of the section. However, the *y*-polarized near fields have approximately equal in-phase and out-of-phase parts, thus suppressing the measured overall SHG signal from component *yxx*. We emphasize that this suppression occurs even though the *x*-polarized input is resonant and the component is allowed. The oscillations caused by *y*-polarized input field, which is nonresonant, result only in weak hot spots at the ends (corners) of the horizontal section. Consequently, the overall SHG signal remains weak for the *yyy* component of sample T_b (Figure 3). The mixed input polarization $x + y$ supports asymmetry of hot spots across the total shape of the particle. Although only the *x*-component of the input field is resonant, the strong asymmetry of the *x*-polarized local field gives rise to a reasonably strong overall signal for tensor component $xxy = xyx$. Importantly, this signal is much stronger than that from the doubly resonant *yxx* component.

The particle shape of sample T_s is similar to that of sample T_b. The main difference is in the vertical section, which is now replaced by a shorter and narrower one. Such a change tunes the *y*-polarized resonance to a shorter wavelength, so that both input polarizations are near-resonant. The *x*-polarized resonance is almost at the same wavelength as for sample T_b and the optical density levels are comparable. Such similarity leads to analogous result for *yxx* component of sample T_s, which is weak due to the cancellation of the SHG fields. For *y*-polarized input field, very strong hot spots appear at the bottom part of the vertical section. The *y*-polarized hot spot is highly asymmetric in *y*-direction, which leads to a strong signal from component *yyy*. As a result, the *yyy* SHG signal from sample T_s is twice as strong as from sample L (Figure 3). Similarly to sample T_b, the input field polarized in $x + y$ direction causes strong asymmetry of hot spots across the entire particle (Figure 4). In this case, both input polarizations are resonant and the fields couple favorably with component $xxy = xyx$, which also leads to twice as strong SHG signal as the dominant signal from sample L. Note also that, compared to the amount of nonlinear material used, sample T_s is about a factor of 2.5 more efficient nonlinear generator than sample L.

The above analysis shows that although L- and T-shaped nanoparticles belong to the same symmetry group and have at least one of the resonances near the fundamental wavelength, the second-harmonic responses from such structures are quite different. In fact, the behavior of the T-shaped nanoparticles is rather peculiar. When illuminated with *x*-polarized light, the SHG signals from relatively strong hot spots cancel, leading to a weak total signal. In other words, this geometry is not favorable for cross coupling between oscillations in the *x*- and *y*-directions, which would be required for the allowed SHG signal represented by component *yxx*. This occurs because the T-geometry allows a direct oscillation along its horizontal section. In this respect, the T-particles behave for *x* polarization very similarly as a plain horizontal bar for which SHG is forbidden by symmetry. Consequently, the existence of a resonance at the fundamental wavelength brings no benefit for the generation of a strong SHG signal. Interesting is also the strong *x*-polarized SHG generated by $x + y$-polarized input field. Some of the local-field components in this case are weaker than under doubly resonant conditions. However, the loss in the strength of the field components is more than compensated by the asymmetry of hot spots, which leads to better optimization of the local-field distributions in the nanostructure. The latter case can be also associated with rotation of polarization in SHG, which is possible for samples of certain symmetry.[42] Our T_s particles do not deviate very much from triangles, which belong to the symmetry group $D_3$. Similarly to the results reported by Konishi et al., T_s is able to rotate incident polarization by 45° in SHG.

In conclusion, we have shown that particle geometry combined with the polarization of the incident field play crucial roles in second-harmonic generation from arrays of metal nanoparticles. The nonlinear response can therefore not be explained simply by plasmonic resonance enhancement of either fundamental or second-harmonic fields, especially when particles of different geometry are compared. In the present work, the most striking result is the symmetry allowed *yxx* component of T-shaped samples. On the basis of resonances and overall symmetry rules only, the SHG signal should be high due to the fact that the fundamental *x*-polarization is resonant and the hot spots of the local field are strong. However, the geometry of the particle leads to cancellation of the strong local signals from the hot spots and thus the overall SHG signal from *yxx* is weak. On the other hand, a weaker field with only one resonant component is sufficient to yield a strong SHG signal. The geometry of the particles therefore supersedes the resonant effects. This issue needs to be carefully considered when new types of nanostructures are designed for strong nonlinear optical responses. In order to obtain efficient strong nonlinear



DOI: 10.1021/nl503901e
*Nano Lett.* 2015, 15, 530−534

response, the geometry of nanostructures needs to be designed to support plasmon resonances and optimized local fields.

## ■ ASSOCIATED CONTENT

### Supporting Information

Table with the details of the plasmon resonances of the samples, the extinction spectra of sample T_s, and the calculated second-harmonic signals at a wavelength slightly detuned from the actual laser wavelength. This material is available free of charge via the Internet at http://pubs.acs.org.

## ■ AUTHOR INFORMATION


### Corresponding Author

*E-mail: robert.czaplicki@tut.fi.

### Present Address

(H.H.) nLIGHT Corporation, Sorronrinne 9, FI-08500 Lohja, Finland


### Notes

The authors declare no competing financial interest.

## ■ ACKNOWLEDGMENTS

This work was supported by the Academy of Finland (132438, 265682). J.M. acknowledges the Graduate School of Tampere University of Technology for funding.

## ■ REFERENCES


(1) Kauranen, M.; Zayats, A. V. *Nat. Photon* **2012**, *6*, 737−748.
(2) Maier, S. A. *Plasmonics: Fundamentals and Applications*; Springer: New York, 2007.
(3) Zhao, L.; Kelly, K. L.; Schatz, G. C. *J. Phys. Chem. B* **2003**, *107*, 7343−7350.
(4) Auguié, B.; Barnes, W. L. *Phys. Rev. Lett.* **2008**, *101*, 143902.
(5) Chu, Y.; Schonbrun, E.; Yang, T.; Crozier, K. B. *Appl. Phys. Lett.* **2008**, *93*, 181108.
(6) Husu, H.; Siikanen, R.; Mäkitalo, J.; Lehtolahti, J.; Laukkanen, J.; Kuittinen, M.; Kauranen, M. *Nano Lett.* **2012**, *12*, 673−677.
(7) Li, K.; Stockman, M. I.; Bergman, D. J. *Phys. Rev. Lett.* **2003**, *91*, 227402.
(8) Stockman, M. I.; Bergman, D. J.; Anceau, C.; Brasselet, S.; Zyss, J. *Phys. Rev. Lett.* **2004**, *92*, 057402.
(9) Canfield, B.; Kujala, K.; Jefimovs, K.; Turunen, J.; Kauranen, M. *Opt. Express* **2004**, *12*, 5418−5423.
(10) Czaplicki, R.; Zdanowicz, M.; Koskinen, K.; Laukkanen, J.; Kuittinen, M.; Kauranen, M. *Opt. Express* **2011**, *19*, 26866−26871.
(11) (a) Klein, M. W.; Wegener, M.; Feth, N.; Linden, S. *Opt. Express* **2007**, *15*, 5238−5247;(b) *Opt. Express* **2008**, *16*, 8055−8055.
(12) Valev, V. K.; Silhanek, A. V.; Verellen, N.; Gillijns, W.; Van Dorpe, P.; Aktsipetrov, O. A.; Vandenbosch, G. A. E.; Moshchalkov, V. V.; Verbiest, T. *Phys. Rev. Lett.* **2010**, *104*, 127401.
(13) Valev, V. K.; Zheng, X.; Biris, C. G.; Silhanek, A. V.; Volskiy, V.; De Clercq, B.; Aktsipetrov, O. A.; Ameloot, M.; Panoiu, N. C.; Vandenbosch, G. A. E.; Moshchalkov, V. V. *Opt. Mater. Express* **2011**, *1*, 36−45.
(14) Valev, V. K. *Langmuir* **2012**, *28*, 15454−15471.
(15) Klein, M. W.; Enkrich, C.; Wegener, M.; Linden, S. *Science* **2006**, *313*, 502−504.
(16) Canfield, B. K.; Husu, H.; Laukkanen, J.; Bai, B.; Kuittinen, M.; Turunen, J.; Kauranen, M. *Nano Lett.* **2007**, *7*, 1251−1255.
(17) Husu, H.; Canfield, B. K.; Laukkanen, J.; Bai, B.; Kuittinen, M.; Turunen, J.; Kauranen, M. *Appl. Phys. Lett.* **2008**, *93*, 183115.
(18) Thyagarajan, K.; Butet, J.; Martin, O. J. F. *Nano Lett.* **2013**, *13*, 1847−1851.
(19) Zhang, Y.; Grady, N. K.; Ayala-Orozco, C.; Halas, N. J. *Nano Lett.* **2011**, *11*, 5519−5523.
(20) Aouani, H.; Navarro-Cia, M.; Rahmani, M.; Sidiropoulos, T. P. H.; Hong, M.; Oulton, R. F. O.; Maier, S. A. *Nano Lett.* **2012**, *12*, 4997−5002.
(21) McMahon, M. D.; Ferrara, D.; Bowie, C. T.; Lopez, R.; Haglund, R. F., Jr. *Appl. Phys., B* **2007**, *87*, 256−265.
(22) Niesler, F. B. P.; Feth, N.; Linden, S.; Wegener, M. *Opt. Lett.* **2011**, *36*, 1533−1535.
(23) Thyagarajan, K.; Rivier, S.; Lovera, A.; Martin, O. J. F. *Opt. Express* **2012**, *20*, 12860−12865.
(24) Park, S.; Hahn, J. W.; Lee, J. Y. *Opt. Express* **2012**, *20*, 4856−4870.
(25) Berthelot, J.; Bachelier, G.; Song, M.; Rai, P.; Colas des Francs, G.; Dereux, A.; Bouhelier, A. *Opt. Express* **2012**, *20*, 10498−10508.
(26) Ross, B. M.; Lee, L. P. *Opt. Lett.* **2009**, *34*, 896−898.
(27) Husu, H.; Mäkitalo, J.; Laukkanen, J.; Kuittinen, M.; Kauranen, M. *Opt. Express* **2010**, *18*, 16601−16606.
(28) Canfield, B.; Kujala, S.; Jefimovs, K.; Svirko, Y.; Turunen, J.; Kauranen, M. *J. Opt. A* **2006**, *8*, S278−S284.
(29) Rao, S.; Wilton, D.; Glisson, A. *IEEE Trans. Antennas Propag.* **1982**, *30*, 409−418.
(30) Umashankar, K.; Taflove, A.; Rao, S. M. *IEEE Trans. Antennas Propag.* **1986**, *34*, 758−766.
(31) Harrington, R. F. *Field Computation by Moment Methods*; Wiley-IEEE Press: New York, 1993.
(32) Aizpurua, J.; Hanarp, P.; Sutherland, D. S.; Käll, M.; Bryant, G. W.; García de Abajo, F. J. *Phys. Rev. Lett.* **2003**, *90*, 057401.
(33) Romero, I.; Aizpurua, J.; Bryant, G. W.; García De Abajo, F. J. *Opt. Express* **2006**, *14*, 9988−9999.
(34) Bryant, G. W.; García de Abajo, F. J.; Aizpurua, J. *Nano Lett.* **2008**, *8*, 631−636.
(35) Kern, A. M.; Martin, O. J. F. *J. Opt. Soc. Am. A* **2009**, *26*, 732−740.
(36) Mäkitalo, J.; Suuriniemi, S.; Kauranen, M. *Opt. Express* **2011**, *19*, 23386−23399.
(37) Forestiere, C.; Capretti, A.; Miano, G. *J. Opt. Soc. Am. B* **2013**, *30*, 2355−2364.
(38) Butet, J.; Gallinet, B.; Thyagarajan, K.; Martin, O. J. F. *J. Opt. Soc. Am. B* **2013**, *30*, 2970−2979.
(39) Wang, F. X.; Rodriguez, F. J.; Albers, W. M.; Ahorinta, R.; Sipe, J. E.; Kauranen, M. *Phys. Rev. B* **2009**, *80*, 233402.
(40) Bachelier, G.; Butet, J.; Russier-Antoine, I.; Jonin, C.; Benichou, E.; Brevet, P.-F. *Phys. Rev. B* **2010**, *82*, 235403.
(41) Butet, J.; Thyagarajan, K.; Martin, O. J. F. *Nano Lett.* **2013**, *13*, 1787−1792.
(42) Konishi, K.; Higuchi, T.; Li, J.; Larsson, J.; Ishii, S.; Kuwata-Gonokami, M. *Phys. Rev. Lett.* **2014**, *112*, 135502.




DOI: 10.1021/nl503901e
*Nano Lett.* 2015, 15, 530−534

Supporting information:

# Second-Harmonic Generation from Metal Nanoparticles: Resonance Enhancement versus Particle Geometry

*Robert Czaplicki*[†], *Jouni Mäkitalo*[†], *Roope Siikanen*[†], *Hannu Husu*[†,‡], *Joonas Lehtolahti*[§], *Markku Kuittinen*[§], *and Martti Kauranen*[†]

[†] Department of Physics, Tampere University of Technology, P. O. Box 692, FI-33101 Tampere, Finland

[‡] nLIGHT Corporation, Sorronrinne 9, FI-08500 Lohja, Finland

[§] Institute of Photonics, University of Eastern Finland, P. O. Box 111, FI-80101 Joensuu, Finland

Corresponding author: robert.czaplicki@tut.fi

**Details of linear spectra**

The linear spectra of the samples, presented in Figure 2 of the main text, were determined by measuring their extinction at normal incidence for *x* and *y* polarizations. In order to facilitate the interpretation of Figure 2, the details of the measured resonances are shown in the Table S1. Note that the important resonances (highlighted) have very similar linewidths, although they differ somewhat in their strengths. In addition, the detuning of the laser from the line center is relatively similar for each resonance.

**Table S1.** Details of the resonances. The highlighted data correspond to the resonances close to the laser wavelength used in the second-harmonic experiments.

| Sample | *x*-polarized resonance | | | | *y*-polarized resonance | | | |
|---|---|---|---|---|---|---|---|---|
| | Resonance wavelength [nm] | FWHM [nm] | Detuning from the 1060 nm | Optical density | Resonance wavelength [nm] | FWHM [nm] | Detuning from the 1060 nm | Optical density |
| L | 1494 | 180 | - | 1.231 | 1023 | 92 | 37 | 1.019 |
| T_b | 1096 | 97 | 36 | 1.143 | 1611 | 244 | - | 1.515 |
| T_s | 1105 | 104 | 45 | 1.19 | 1023 | 100 | 37 | 0.68 |

**Simulation of second-harmonic generation**

In order to support the results obtained in the experiments, both the linear and nonlinear responses from the samples were simulated using the boundary element method (BEM).

Reliable simulation of the second-harmonic generation (SHG) signals requires very good agreement between the measured and calculated polarized extinction spectra. Although the overall agreement in our case is very good even on a quantitative level, small differences do appear at the fundamental wavelength used in the SHG experiments (1060 nm). These differences are particularly important for the sample T_s, where both *x* and *y* polarizations are near resonant (Figure S1).

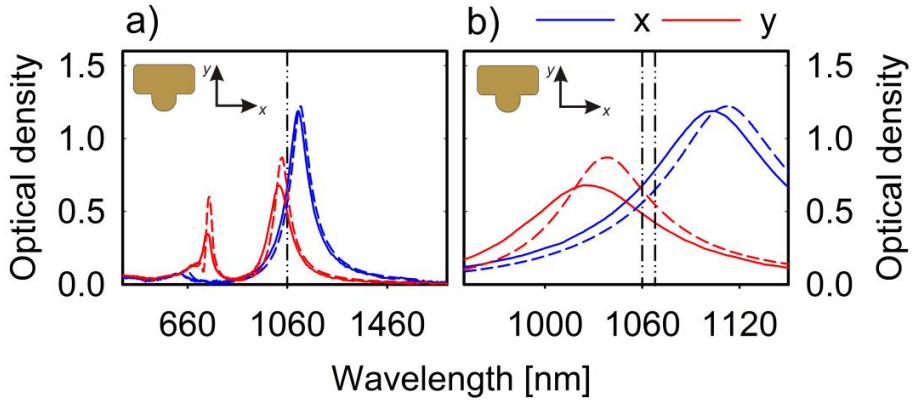


**Figure S1.** Polarized extinction spectra of sample T_s: a) full spectrum b) narrower range to show details of resonances and optical density levels at both used wavelengths. The solid lines denote measured spectra and dashed lines the calculated ones. The fundamental wavelength of our laser (1060 nm) is marked as vertical dash-dotted line. The second dash-dotted line in part a) shows wavelength (1068 nm) used for repeated calculations.

In order to show how such minor differences can influence the simulated SHG, we repeated the calculations for the wavelength (1068 nm) which represents qualitatively similar relative optical densities in simulations as measured in the experiment for our laser wavelength (1060 nm). The SHG signals simulated for 1068 nm fundamental wavelength (Figure S2) show even better agreement with the experimental data.

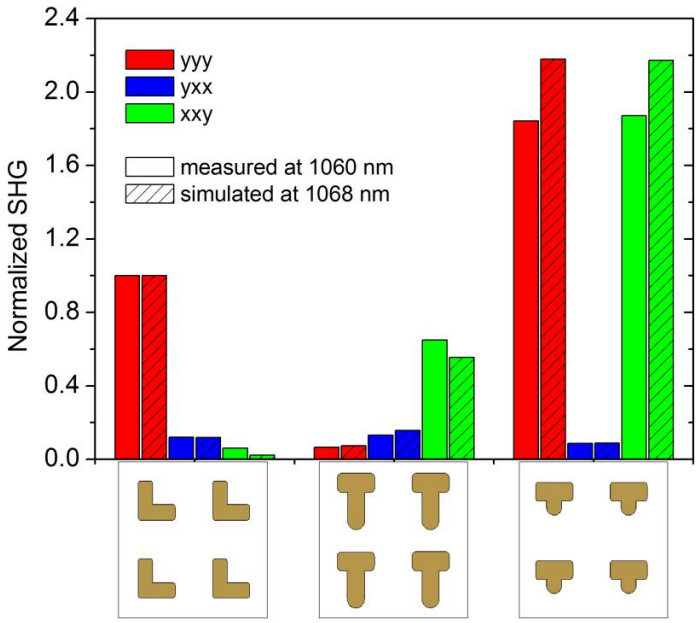


**Figure S2.** SHG signals from studied samples normalized to *yyy* component of sample L. The non-patterned bars represent experimental data (fundamental wavelength 1060 nm) and the patterned bars show calculated signals (fundamental wavelength 1068 nm).